

1 **Determining spatio-temporal characteristics of Coseismic Travelling**
2 **Ionospheric Disturbances (CTID) in near real-time**

3
4 Boris Maletckii* & Elvira Astafyeva

5 *Université de Paris, Institut de Physique du Globe de Paris (IPGP), CNRS UMR*
6 *7154, 35-39 Rue Hélène Brion, 75013 Paris*

7 *Corresponding Email: maletckii@ipgp.fr*

8

9

10 **ABSTRACT**

11 Earthquakes are known to generate ionospheric disturbances that are commonly
12 referred to as co-seismic travelling ionospheric disturbances (CTID). In this work, for
13 the first time, we present a novel method that enables to automatically detect CTID in
14 ionospheric GNSS-data, and to determine their spatio-temporal characteristics
15 (velocity and azimuth of propagation) in near-real time (NRT), i.e., less than 15
16 minutes after an earthquake. The obtained instantaneous velocities allow us to
17 understand the evolution of CTID and to estimate the location of the CTID source in
18 NRT. Furthermore, also for the first time, we developed a concept of real-time travel-
19 time diagrams that aid to verify the correlation with the source and to estimate
20 additionally the propagation speed of the observed CTID. We apply our methods to
21 the Mw7.4 Sanriku earthquake of 09/03/2011 and the Mw9.0 Tohoku earthquake of
22 11/03/2011, and we make a NRT analysis of the dynamics of CTID driven by these
23 seismic events. We show that the best results are achieved with high-rate 1Hz data.
24 While the first tests are made on CTID, our method is also applicable for detection
25 and determining of spatio-temporal characteristics of other travelling ionospheric
26 disturbances that often occur in the ionosphere driven by many geophysical
27 phenomena.

28

29 **Keywords:** ionosphere, GNSS, earthquakes, TEC, TIDs, real-time

30

31

32

33

34 Introduction

35 It is known that natural hazard events, such as earthquakes, tsunamis and/or
36 volcanic eruptions generate acoustic and gravity waves that propagate upward in the
37 atmosphere and ionosphere [e.g., 1; 2 ;3 ;4 ;5 ;6 ;7]. Earthquake-driven ionospheric
38 disturbances are called co-seismic travelling ionospheric disturbances (CTID). The
39 first CTID are generated directly by the ground or the seafloor via acoustic waves,
40 they reach the ionospheric altitudes (~200-350 km) in only 7-9 minutes. They are
41 followed by acoustic waves generated by the surface Rayleigh waves, tsunami
42 gravity waves. Nowadays, with the development of permanent networks of dual-
43 frequency Global Navigation Satellite Systems (GNSS) receivers, the detection of
44 CTID and other Natural-Hazard-driven (NH-driven) ionospheric perturbations has
45 nowadays become quite regular [e.g., 8; 9; 10; 11; 5; 12].

46 Recently, it has been suggested that NH-driven ionospheric disturbances can be
47 used for more advanced purposes: to localize NH and to estimate the characteristics
48 of the source [e.g., 13; 9; 4; 14; 15; 16; 17; 18; 19]. Kamogawa *et al.* [20] suggested
49 a method based on observations of a “tsunami-ionospheric hole”, ionospheric
50 depletion that often occurs after major earthquakes over the epicentral area. Based
51 on the analysis of seven tsunamigenic earthquakes in Japan and Chile, Kamogawa
52 *et al.* [20] found a quantitative relationship between the initial tsunami height and the
53 TEC depression rate. Manta *et al.* [21] developed a new ionospheric tsunami power
54 index based on measurements of CTID. They showed that the ionospheric index
55 scales with the volume of water displaced due to an earthquake. However, neither of
56 these methods is real-time compatible. As near-real-time (NRT) mode, we refer to as
57 10-15 minutes after an earthquake. Going further towards NRT, Savastano *et al.* [22]
58 made the first preliminary feasibility demonstration for ionospheric monitoring by
59 GNSS, by developing a software VARION that can derive TEC in NRT. Their
60 technique has been implemented at several GNSS-receivers around the Pacific
61 Ocean (<https://iono2la.gdgps.net>), and is aiming - in the future - to detect traveling
62 ionospheric disturbances (TIDs) associated with tsunamis. Shrivastava *et al.* [23]
63 demonstrated the possibility of tsunami detection by GPS-derived TEC, however, no
64 discussion on the real-time use was provided.

65 Ravanelli *et al.* [24] claimed to provide the first real-time ionosphere-based
66 tsunami risk assessment by data GNSS receivers in Chile. However, they analyse 2
67 hours of data and used 8th order polynomial, i.e., their approach requires stacking of

68 about 2 hours of data. Therefore, this approach is not NRT-compatible by our
69 definition.

70 Therefore, recent seismo-ionospheric results show a big potential for the future
71 use of ionospheric measurements for natural hazard risk assessment. However,
72 before such methods could be applied in real-time, several major developments are
73 yet to be implemented. Going toward real-time applications, the first step is to
74 automatically detect CTID in near-real-time and to analyze their features in order to
75 prove their relation to earthquakes. In this work, we introduce, for the first time, near-
76 real-time compatible methods for determining the spatio-temporal characteristics of
77 CTID.

78

79 **Methods**

80 **1. Estimation of Total Electron Content (TEC) from GNSS**

81 GNSS allows to estimate the ionospheric total electron content (TEC), which is
82 an integral parameter equal to the number of electrons along a line-of-sight (LOS)
83 between a satellite and a receiver. The LOS TEC is often called slant TEC (sTEC).
84 The TEC is usually measured in TEC units (TECU), with 1 TECU equal to 10^{16}
85 electrons/m². To calculate the TEC, one needs phase and code measurements
86 performed by dual-frequency receivers [i.e., 25]. However, the code measurements
87 are only needed to remove the inter-frequency bias. While, the co-seismic signatures
88 and other disturbances can be retrieved from phase TEC estimated solely from
89 phase measurements:

$$90 \quad sTEC_{ph} = \frac{1}{A} \cdot \frac{f_1^2 f_2^2}{f_1^2 - f_2^2} (L_1 \lambda_1 - L_2 \lambda_2) \quad (1)$$

91

92 where $A = 40.308 \text{ m}^3/\text{s}^2$, L_1 and L_2 are phase measurements, λ_1 and λ_2 are
93 wavelengths at the two Global Positioning System (GPS) frequencies (1227,60 and
94 1575,42 MHz). Therefore, in near-real-time approach approach, we will only use
95 these phase measurements that can be easily transferred in very short time (Figure
96 1). The first data point is removed from the whole data series as the unknown bias.

97 In order to determine the position of ionospheric disturbances, we estimate the
98 coordinates of so-called sub-ionospheric points (SIP) that represent the intersection
99 points between the LOS and the ionospheric thin shell. The satellite orbit information
100 can be rapidly transferred in NRT from the IGS in navigation RINEX files (Figure 1),

101 or it can be forecasted very precisely based on the current known satellite
102 coordinates. Otherwise, ultra-rapid orbits can be used. The shell altitude H_{ion} is not
103 known but presumed from physical principles: we expect the observed perturbation
104 to be concentrated at the altitude of the ionization maximum (HmF2). In NRT, the
105 value of HmF2 can be obtained either from nearest ionosonde stations, or from
106 empirical ionospheric models, such as NeQuick [26] or International Reference
107 Ionosphere (IRI) [27]. Here we take $H_{ion} = 250$ km, which is close to the HmF2 on
108 the days of the earthquakes [15; 28].

109 It should be noted that in the vast majority of previous studies of ionospheric
110 response to earthquakes the researchers used band-pass filters, such as running
111 mean, polynomial fitting, high order Butterworth, etc. [e.g., 29; 30; 31]. However, in a
112 real-time scenario one cannot use such filters because of the impossibility to stack
113 long series of data (up to 30-60 min) and due to the lack of time. In addition, the
114 band-pass filtering would induce artefacts and will affect the properties of the
115 detected signals (arrival time, amplitude, spectral components). Therefore, here we
116 suggest to analyze the rate of TEC change ($dTEC/dt$) instead of the sTEC. Such a
117 derivative procedure works as a high-pass filter and removes the bias and trend
118 caused by the satellite orbit motion. In addition, our $dTEC/dt$ approach will not modify
119 the amplitude of CTID.

120 Below we use 1Hz GNSS data for our real-time scenario.

121

122

123 **2. Real-time detection of co-seismic travelling ionospheric disturbances** 124 **from TEC data series**

125 The concept of the developed method is presented in Figure 2. CTID is
126 detected by analysing the sTEC data series by 5-sec centered moving averaged over
127 a 5-min window. The averaging prevents detection of random peaks in data. The
128 window duration is chosen to be NRT-compatible and, at the same time, it allows
129 more thorough analysis of CTIDs characteristics in multiple data series at later steps.
130 Within the selected time window, we search for a local maximum value (LMV) that
131 must exceed every other value within the window.

132 At step #2, within the window, we switch from sTEC to $dTEC/dt$. With such an
133 approach, we focus on sudden strong co-seismic TEC signatures that are analogous
134 to the peak ground displacements [32]. Figure 3(a) shows examples of CTID

135 detected by GPS stations 0980, 3007 after the 2011 Tohoku-oki earthquake (1Hz
136 data). The co-seismic signatures in sTEC data series (panels **a**, **b**) are quite
137 significant, however, the presence of the trend makes it difficult to calculate the
138 correlation function and the time shift between the data series that are necessary at
139 later steps. In turn, in the dTEC/dt data series, the CTID signatures are visible, but
140 the trend is removed (Figure 3c). The chosen 5-minute window is enough to compute
141 the correlation, since it catches the CTID signatures and they prevail in the time
142 span.

143 At step #3, we compute the cross-correlation function for two data series in
144 order to obtain the time shifts in the signal arrivals. The latter is found based on the
145 maximum of the cross-correlation function. In addition, the cross-correlation can
146 correct possible errors in finding the LMV. Finally, from the obtained maximum
147 values, it can select 3 GNSS stations for the D1- technique, as explained below in
148 P.3.

149 To calculate the cross-correlation function, we use Fast Fourier
150 Transformation (FFT), which is a rapid procedure and suitable for NRT applications.
151 Figure 3d shows an example of the cross-correlation function between dTEC/dt data
152 series at two GPS receivers.

153 The threshold for the correlated data series depends on the standard deviation
154 of dTEC/dt series:

$$155 \quad T = 1 - (1 - K * \sigma_1) * (1 - K * \sigma_2) \quad (2)$$

156 where σ_1, σ_2 - the standard deviation of dTEC/dt series at GNSS sites. The
157 standard deviation is an indicator of data noisiness. The noisier the data the more
158 difficult it is to detect CTID because of a lower correlation coefficient. Therefore, our
159 approach will adaptively consider the data noise level. Another issue in determining
160 the threshold T is linked with different data cadences. The dTEC/dt values will
161 increase with data cadence. Consequently, to adapt the threshold estimation to
162 different data sampling, we introduce a normalizing coefficient K . For 1-Hz data, the
163 K is chosen to be 10 TECu^{-1} based on data analysis. Such an adaptive approach
164 makes our method adjustable to the scale of an ionospheric response and aids to
165 automate the triangle selection process (at a later step). It is known that smaller
166 earthquakes generate CTID of smaller amplitudes [15]. When the response is
167 weaker, the threshold is smaller due to smaller the standard deviation of dTEC/dt

168 series and vice versa. (Figure S1). Setting a constant threshold may affect the results
169 and that there is a need for an adaptive algorithm for this problem.

170

171 **3. Real-time estimation/determining of spatio-temporal parameters. D1-**

172 **GNSS-RT method**

173 To determine spatio-temporal parameters of CTID, such as the horizontal velocity
174 and the azimuth of propagation, we use a so-called “D1” method. This is an
175 interferometric approach that was introduced by Afraimovich *et al.* [33] to analyze
176 and detect TIDs, of which CTIDs are a subclass. Originally, this method was based
177 on use of GPS-measurements only [33; 34]. Our method works with all GNSS data,
178 and it is real-time compatible, therefore, we refer to it as “D1-GNSS-RT”.

179 The disturbances detected by a system of three spatially separated receivers,
180 that act as an interferometric system, are considered to be parts of the same
181 wavefront (Fig. 4a). Then, by analysing the wave characteristics (such as phase,
182 frequency, signal amplitude) of the observed disturbances, we determine the time
183 shift between CTID arrivals at the detection “triangle”. Three assumptions are used in
184 the subsequent calculations: 1) the wave front is plane, i.e., the distance between the
185 receivers is less than the horizontal dimensions of CTID; 2) the wave front is
186 homogenous; 3) the CTID propagates horizontally i.e. the GNSS-receivers detect the
187 perturbations at the same altitude (*Hion*).

188 At the “0” time moment, a disturbance with horizontal velocity v_h and azimuth α
189 is approaching the “A-B-C” interferometric system. At the moment “I”, the CTID is
190 detected by the receiver “A”, and it is further moving to other receivers of the system.
191 It is important to note that the consideration of the wave front as plane and
192 homogeneous means that both v_h and α would not change when the CTID arrives at
193 the other points of the given system. Garrison *et al.* [35] showed the correctness of
194 such an assumption for small-scale (3-10 minutes) TIDs, based on the dense
195 network of receivers in the limited space. At moment “II”, the CTID has already
196 passed receiver “A”, and arrived at receiver “B”. At “III”, the CTID arrives at receiver
197 “C”. Only after this step, one can compute the characteristics of the perturbation. The
198 velocity v_h and the azimuth α are then estimated by using the following formulas [36]:

199
$$u_x = \frac{x_A y_C - x_C y_A}{y_C (t_A - t_B) - y_A (t_C - t_B)} \quad (3)$$

200
$$u_y = \frac{x_A y_C - x_C y_A}{x_A (t_C - t_B) - x_C (t_A - t_B)} \quad (4)$$

201
$$v_h = \frac{u_x * u_y}{\sqrt{u_x^2 + u_y^2}} \quad (5)$$

202
$$\tan \alpha = \frac{u_y}{u_x} \quad (6)$$

203

204 For better spatial representation, the location of the obtained horizontal
205 velocity vector is placed at the point with the first arrival of the disturbance (point A in
206 Figure 4a). While, in the temporal domain, the obtained velocity is linked with the
207 arrival time of the disturbance at point C.

208 As mentioned before, the D1-method is only applicable to a TID with a plain
209 waveform. It is known however that, in most cases, the wave front of CTID is circular
210 [e.g., 5; 37]. Therefore, the farther are the stations from one other, the worse is the
211 plain wave condition fulfilled. Also, larger distance between the stations will lower the
212 maximum of the cross-correlation function. Consequently, the D1-GNSS-RT can only
213 be used on a very small segment of the circular wavefront. This limitation requires
214 additional analysis of the positions of the A, B, C receivers with respect to the
215 wavefront. To do that, here we use the cross-correlation function that is the criterion
216 of the similarity of multiple data series. It should be noted that the waveform of the
217 CTID largely depends on the conditions of observations, such as magnetic field
218 configuration in the epicentral area, geometry of GNSS-sounding and the
219 background ionization [e.g., 37; 38; 39; 40]. Therefore, only perturbations registered
220 close to one another will have similar waveforms.

221

222 **4. Localization of the source of ionospheric disturbances**

223 The velocity field obtained by the D1-GNSS-RT method can further be used to
224 locate the source of TIDs. The source is defined as a point in the ionosphere where
225 the CTID generated and starts to propagate. We switch to Latitude-Longitude
226 coordinate system, where x-axis is directed from West to East and y-axis is directed
227 from North to South (Fig. 4b). We take the azimuths (α_i) and the values (v_i) of the
228 velocities, as well as the coordinates (lon_{0i} and lat_{0i}) of the velocity “vectors” from
229 the output of the D1-GNSS-RT. This gives us a linear system, where the coordinates
230 (lon_0 and lat_0) of the source of ionospheric disturbances are unknown. There are two
231 additional restrictions on the system solutions: 1) the horizontal distance between the
232 vectors should be less than 50 km and 2) the difference in the arrival times between

233 points A-B and A-C should be less than 30%. These restrictions are thought to avoid
 234 the location of velocity vectors to be on the same segment of the CTID wavefront in
 235 order to fulfill the condition of the plain wavefront.

236 For one velocity vector the distance to the source is defined by the following
 237 equation (Fig. 4b):

$$238 \quad \quad \quad lon_0 - lon_{0i} = \tan(\alpha_i) * (lat_0 - lat_{0i}) \quad (7)$$

239 Where, lon_0 and lat_0 – the coordinates of the source, lon_{0i} and lat_{0i} - that of the
 240 given velocity vector, α_i – the azimuth of the velocity vector. Similarly, for two vectors
 241 we obtain:

$$242 \quad \quad \quad \begin{cases} lon_0 = \tan(\alpha_1) * (lat_0 - lat_{01}) + lon_{01} \\ lon_0 = \tan(\alpha_2) * (lat_0 - lat_{02}) + lon_{02} \end{cases} \quad (8)$$

243 Based on the system above, the coordinates of the intersection of the two vectors
 244 can be estimated as:

$$\begin{cases} lat_0 = \frac{(lon_{02} - lon_{01}) + (lat_{01} * \tan(\alpha_1) - lat_{02} * \tan(\alpha_2))}{\tan(\alpha_1) - \tan(\alpha_2)} \\ lon_0 = lon_{01} + \tan(\alpha_1) * (lat_0 - lat_{01}) \text{ or } lon_{02} + \tan(\alpha_2) * (lat_0 - lat_{02}) \end{cases} \quad (9)$$

245
 246 Once the source location is known, along with the velocity vector location and
 247 its value, the onset time of the source is estimated as follows:

$$248 \quad \quad \quad t = t_i + \Delta t_i \quad (10)$$

249 Where, t_i is the time of the velocity vector and Δt_i is defined by:

$$250 \quad \quad \quad \Delta t_i = \frac{Dist(lon_0, lat_0, lon_{0i}, lat_{0i})}{v_i} \quad (11)$$

251 Where, $Dist(lon_0, lat_0, lon_{0i}, lat_{0i})$ is the distance between the source location and
 252 the velocity vector location. If the difference in determination of the source onset time
 253 from the two given velocities is less than the sampling interval, we consider this pair
 254 of velocities as a possible solution for a specific moment of time and location of the
 255 source.

256
 257

258 Results

259 We apply our newly developed methods to the cases of two shallow (~32km)
 260 earthquakes that occurred in March 2011 off the east coast of Honshu, Japan. The
 261 first one is the great M9.1 Tohoku-oki earthquake. According to the US Geological
 262 Survey (The National Earthquake Information Center

263 (NEIC); <http://earthquake.usgs.gov>), the epicenter of this earthquake was located
264 at 38.322°N and 142.369°E (Fig. 5a), and the onset time was estimated at 05:46:26
265 UT. The rupture lasted about 180 seconds, and caused significant co-seismic
266 cumulative slip with the maximum of 56 m on the north-east from the epicentre
267 (Figure 5a) [41]. Several research groups pointed out that the Tohoku earthquake
268 slip consisted of 2 or 3 “segments” [e.g., 42; 43], that present multiple sources for the
269 ionospheric disturbances [e.g., 19].

270 The second event is the M7.3 Sanriku-oki earthquake that occurred 55 hours
271 before the Tohoku earthquake (i.e., on 9 March) and is often referred to as the
272 Tohoku foreshock. According to the USGS, the rupture started at 02:45:20 UT at the
273 epicentre with coordinates: 38.435°N, 142.842°E (Fig. 5b). This smaller event lasted
274 30-40 seconds and provoked a 2 m co-seismic slip on the north-west from the
275 epicentre (Figure 5b) [44].

276 To analyze the CTID activity, in both cases, we apply our method to 1Hz
277 GNSS ionospheric data from the Japan GNSS Earth Observation Network
278 (GEONET, <https://www.gsi.go.jp>).

279

280

281 **1. The velocity field and ionospheric localisation of the 2011 M9.1 Tohoku-** 282 **oki earthquake**

283 The ionospheric response to the Tohoku earthquake was studied in detail by
284 numerous research teams [e.g., 6; 5; 14; 15; 19]. As shown in Figure 3, the near-
285 field TEC response showed very complex waveforms, with several peaks in TEC
286 data. The amplitude of this response was also quite significant as compared to other
287 earthquakes and was detected by ten GPS satellites [45; 46; 47]. Here we work with
288 data of GPS satellite 26 that showed the largest and the clearest co-seismic
289 signatures.

290 The CTID velocity field maps for the first CTID arrivals following the Tohoku
291 earthquake are shown in Figures 6a-d, and the localization results are shown in
292 Figure 6e-h. It should be noted that, in principle, we can calculate the CTID
293 characteristics for multiple periods of time, as long as the perturbations are detected.
294 For the Tohoku event, instantaneous velocity maps for the first 2 minutes of CTID
295 detection can be found in Animation S1 (available as supplementary material), and
296 the localization results are shown in Animation S2 (supplementary material). Figure

297 6a shows the first velocity vectors at 05:54:13UT, i.e. 487 seconds after the
298 earthquake onset time, on the north-east from the epicenter. The first vectors are
299 directed south-westward, and the first points have the velocities of about 4 km/s.
300 Such velocity values might correspond to the propagation of the primary (P-) seismic
301 waves (i.e., the rupture propagation), or to the propagation of the Rayleigh surface
302 waves. These first velocity vectors give the first source location at the point with
303 coordinates (38.18; 143.55) (Figure 6e). At 05:54:57UT, one can see further
304 development of the CTID evolution within the source area, with smaller velocities. In
305 addition, we notice the occurrence of the second source on the south-east from the
306 epicentre (Figures 6b,f). Further, one can clearly see the occurrence of the second
307 segment of the source on the south-east from the epicenter (Figures 6d,g). At
308 05:56:10UT, we observe further evolution of CTID, and westward propagation of
309 CTID with velocities from 600 m/s to ~3 km/s. This range of velocities was previously
310 observed for the CTID generated by the Tohoku earthquake [e.g., 6; 5; 14].

311 The CTID propagation speed can be verified by plotting so-called travel-time
312 diagrams (TTD), that present 3-D diagrams with the distance from the source versus
313 time after the source onset, and the amplitude of CTID is shown in color. TTD also
314 enable to confirm the correlation of the observed perturbations with the source. In
315 retrospective studies, a band-pass filter was applied in order to better extract the co-
316 seismic signatures and to clearly see the correlation with the source. In NRT mode,
317 and with the impossibility to use such a filter, we suggest using $dTEC/dt$ parameter,
318 and we call such diagrams near-real-time TTD (NRT-TTD). This is the first NRT-
319 compatible method proposed for obtaining the TTD. As a source, at the first
320 approximation, we can take the epicentre position that should be known from
321 seismological data several minutes after the earthquake. However, the epicentre is
322 the point where the rupture starts, and its position does not always correspond
323 (especially for large earthquakes) to the position of the co-seismic crustal uplift that
324 generates CTID as well as tsunamis. The problem lies, however, in the fact that in
325 NRT, it is very difficult to know the position of the uplift or the slip. Therefore, we can
326 take the position of the source estimated from our ionospheric methods.

327 The NRT-TTD for the Tohoku event, G26 satellite, plotted for the source
328 located at the epicentre, the center of the maximum slip (38.64; 143.35) and the
329 "ionospheric source" (37.944; 143.153) are presented in Figure 7a,b,c, respectively.
330 It should be noted that the Tohoku earthquake produced significant displacement of

331 the ground on a large area (the approximative fault size is about 300*80km) and,
332 strictly speaking, taking a single point as the source is an approximation. However,
333 we proceed with such an assumption to plot the NRT-TTD. The correlation is seen
334 when CTID propagates “linearly” from the source. Comparison of Figures 7a, 7b and
335 7c reveals that the best correlation is obtained for the slip maximum (Figure 7b) and
336 for the ionosphericly-determined source (Figure 7c). While, the perturbation is not
337 well-aligned when the diagram is plotted with respect to the epicentre (Figure 7a).
338 The propagation speed of the observed CTID can be estimated from the slopes on
339 the TTD. We find the speeds to be ~2.3-2.6 km/s, which is in line with previous
340 retrospective observations for the ionospheric response to the Tohoku earthquake
341 [e.g., 6; 5; 14; 15].

342

343

344 **2. The velocity field and ionospheric localisation of the 2011 M7.3 Sanriku-** 345 **oki earthquake**

346 Ionospheric response to the Sanriku earthquake was studied previously by
347 Thomas *et al.* [48] and Astafyeva & Shults [28]. The co-seismic TEC signatures were
348 detected by satellites G07 and G10. Here we only focus on CTID registered by GPS
349 satellite G07. Contrary to the CTID generated by the Mw9.0 Tohoku earthquake, the
350 ionospheric TEC response to this smaller earthquake presented the commonly
351 known N-wave signatures with smaller amplitudes. However, even despite the
352 smaller amplitude of CTID, our method detects these disturbances.

353 The instantaneous velocity field maps are presented in Figure 8a-d. One can
354 notice that the picture of the velocity field for the CTID generated by the Sanriku
355 event is much simpler than the one for the Tohoku event. The first velocity vector is
356 shown at 02:55:08UT, i.e. 588 seconds after the earthquake onset time. At that
357 instant, the CTID starts to propagate south-westward at the velocity of about 850 m/s
358 (Figure 9a). Within the next minute, we observe south-westward propagation of
359 ionospheric disturbances at ~850-1100 m/s (Figures 8b-c). At 02:56:08UT, we further
360 observe further southwestward propagation of CTID (Figure 8d). From these first
361 velocity fields, we estimate the location of the source to be on the south-east from the
362 epicentre (Figures 8e-h). Overall, one can notice significant difference in the velocity
363 field and CTID evolution during this smaller earthquake. The CTID has lower

364 velocities, and the velocity field is much less complex as compared to the Tohoku
365 earthquake.

366 The corresponding RT-TTD calculated with respect to the epicentre, the
367 maximum slip point (38.5; 142.7), and the ionospherically determined (38.335;
368 143.442) source are presented in Figure 7d,e,f, respectively. The best alignment is
369 achieved for the ionospheric source (Figure 7e), where we also see concurrent
370 northward and southward propagation from the source. While, for the two other
371 sources one cannot clearly see this effect (Figures 7a and 7e). Therefore, our results
372 suggest that the source was located on the south-east from the epicentre. The worst
373 alignment is obtained for the epicentre as the source of CTIDs (Figure 7d). The CTID
374 propagation speed is estimated to be 1.2-1.6 km/s, which is close to the estimation in
375 after-earthquake analysis by Astafyeva and Shults [28].

376

377 **Discussions**

378 Above we demonstrated the possibility to calculate in NRT spatio-temporal
379 characteristics of CTIDs on the example of two earthquake events that occurred in
380 Japan in March 2011. For both earthquakes, we also localized in NRT the source of
381 the observed CTIDs. It should be reminded that the CTID coordinates and,
382 consequently, the estimated position of ionospheric sources will change if we vary
383 the altitude of detection *Hion*. In this work, we took $Hion = 250\text{km}$, which is close to
384 the ionization maximum in the epicentral areas during the earthquakes, and is the
385 right choice from a physical point of view. However, recently it has been suggested
386 that the actual GNSS detection of CTID may take place at lower altitudes [48; 28;
387 19]. Therefore, strictly speaking, the *Hion* should be determined each time for the
388 correct estimation of the CTID coordinates. Our method is fully operational
389 independently on the *Hion* value, however, its results and the accuracy of the
390 ionospheric source localization might be improved if/when we know the real *Hion*.
391 Determining the exact altitude of detection is out of the scope of the current work.

392 Here we used 1Hz GNSS TEC data from the Japanese network of GPS
393 receivers GEONET, i.e. a network with good spatial coverage with 20-km distance
394 between the receivers, and we demonstrated that in such observational conditions,
395 our NRT-compatible methods provide good results both in terms of the source
396 localisation and determining of CTID spatio-temporal characteristics. In our method,
397 the accuracy of localisation seems lower than that by seismic stations that invert the

398 position of the epicentre based on detection of seismic waves. The seismic source
399 can also be localized by other non-seismic instrumentation, such as by balloon
400 pressure sensors via detection of infrasound signals due to earthquakes. For
401 instance, Krishnamoorthy *et al.* [49] showed that the source can be localized with
402 90% probability within an ellipse with a semimajor axis approximately 80 m under the
403 perfect conditions. They used 26 shots that is equal to the usage of a 26-balloon
404 array to solve this task. It should be noted, however, that this result was obtained by
405 a-posteriori analysis, therefore it might be quite challenging to repeat such quality in
406 NRT.

407 Further, we discuss how lower or much lower spatial and temporal resolutions
408 of GNSS ionospheric data could affect the output of our methods. Also, the accuracy
409 of estimation of the velocities and the source location should be determined.

410 With regards to the data sampling, for both earthquakes, we tested our
411 methods on 30-sec data that are available from the GSI
412 (http://datahouse1.gsi.go.jp/terras/terras_english.html). We have found that such a
413 resolution is not enough because of two main reasons. First, fewer data within the
414 selected window duration of 5 min will smooth the dTEC/dt values, which, in turn, will
415 erase the specific features of CTIDs that characterize different segments of the
416 wavefront. As mentioned before, the D1-GNSS-RT method can only be used on a
417 small part of a wavefront, because it is only applicable to the plain wave. Therefore,
418 with 30-sec data sampling, it is difficult to control this condition in terms of the
419 correlation between data series, especially for smaller earthquakes, for which the
420 response is smaller in amplitude and duration [46]. Second, 30-sec data rate will
421 introduce ± 15 -sec error in the LMV determining within the window, and,
422 consequently, it will lead to errors in the arrival time at each point of a triangle. The
423 impact of such ± 15 -sec error can be seen in Figure 9a-b, where we present the
424 normalized number of the time shifts between points A-B (red, ΔT_1) and A-C (blue,
425 ΔT_2) of a triangle for the Tohoku (a) and Sanriku (b) earthquakes. For both events,
426 the distribution of ΔT_1 and ΔT_2 have the same shape and look quite similar, but are
427 shifted for ~ 5 seconds. This emphasizes the fact that a CTID arrives at points B and
428 C at close moments of time, that is only possible if the arrivals belong to the same
429 segment on a circular disturbance wavefront. One can also notice that, for both
430 events, the majority of arrivals are registered within a narrow period of time, 20 to 40

431 seconds for the Sanriku event (Figure 9a) and 25 to 60 seconds for the Tohoku event
432 (Figure 9b). This means that lower time steps in data will lead to errors in the correct
433 detection of the moment of arrival would occur, and, consequently will eventually
434 impact the velocity values and the azimuths.

435 To further analyze the applicability of our method to lower cadence data, we
436 downsampled the initial 1Hz data to 5-, 10- and 15-sec cadence. Figure 10 shows
437 how different data cadences impact the distribution of calculated velocities. One can
438 see a significant difference in the results for 1sec and 30 sec data. Therefore, for
439 better performance of our methods we suggest the use of GNSS-data with 1Hz
440 sampling.

441 With respect to the accuracy of our method, we analyzed how an error of ± 0.5
442 seconds in arrival times affects the computation of the velocity values and azimuths.
443 The normalized number of error cases versus the absolute error percentage is shown
444 in Figure 9c. One can see that $\sim 80\%$ of both velocities and azimuths have less than
445 2.5% of errors and $\sim 95\%$ - less than 5%. These results also confirm the advantage of
446 high-rate data.

447 The use of different orbital information can impact the accuracy of our method,
448 because the coordinates of CTID depend on the position of a satellite as well as of
449 that of a GNSS station. The commonly used ephemerides are those transferred in
450 the RINEX navigation file. Alternatively, ultra-rapid orbits can be used. We compared
451 the amplitude and direction of the obtained velocity vectors based on ultra-rapid
452 orbits with those calculated based on the use of the RINEX navigation files (Fig
453 11a,b). Then, we computed source locations based on these velocities and
454 estimated the error in position (Fig 11c,d). This analysis was made both for the
455 Tohoku and the Sanriku cases. One can see that the majority of both velocities and
456 azimuths have less than 0.05% of differences. This fact can be explained by the high
457 quality (cm-accuracy) of the real-time IGS products [50]. However, the radar
458 diagrams of error positioning show worse results (Figure 11c,d).

459 Finally, we would like to note that our methods can be used for detection of
460 TIDs of other origins in addition to CTID and, therefore, it is useful for real-time
461 Space Weather applications. The D1-GNSS-RT will automatically catch all CTID and
462 TID with high $d\text{TEC}/dt$ values, where the maximum disturbance amplitude exceeds
463 the noise level by at least 4 times (Figure S4a). Such disturbances could be
464 generated by acoustic or gravito-acoustic waves (earthquakes, volcanic eruptions,

465 rocket launches), or by enhanced EUV radiation (solar flares) that produces rapid
466 growth of the ionization in the ionosphere (Figure 12). It should be emphasized that
467 for the detection, the absolute amplitude of CTID and TID is less important than the
468 $dTEC/dt$. For instance, it is known that smaller earthquakes generate smaller
469 disturbances in the ionosphere [15; 47]. Therefore, it is of interest to apply our
470 technique to the smallest earthquake ever recorded in the ionosphere – the M6.6 16
471 July 2007 Chuetsu earthquake in Japan [47]. The Chuetsu earthquake produced a
472 very small-amplitude TEC disturbance that was registered by satellite G26 and by a
473 few GPS-stations in the near-epicentral region, and the only data available were of
474 30-sec cadence. Unfortunately, the latter factors did not allow us to compute the
475 velocities and the localization by using the D1-GNSS-RT technique. However, our
476 method successfully found the LMV even for such a small CTID but with sufficient
477 $dTEC/dt$ rate (Figure S5b,c). Also, Figure S5 demonstrates that we could track the
478 CTID propagation with respect to the source in NRT by using our RT-TTD technique.

479 On the other hand, disturbances with lower $sTEC$ derivative or/and higher
480 noise level might appear undetectable or the D1 triangles will not be formed because
481 of low cross-correlation between data series. For instance, we did not manage to
482 catch CTID registered by satellites G27 (during the Tohoku earthquake) and G10
483 (during the Sanriku earthquake), because they had low $dTEC/dt$. Another example is
484 the ionospheric response to the M7.8 2016 Kaikoura earthquake that occurred on 13
485 November 2016 in New Zealand, for which we also analysed high-rate 1Hz data. The
486 latter TEC variations presented more noise and the amplitude of the detected CTID
487 did not grow up as fast as for the Tohoku and Sanriku cases (Figure S4). For such
488 less pronounced disturbances, other more sophisticated methods should be
489 developed, which is a subject of a future separate work.

490

491 **Conclusions**

492 For the first time, we introduce a NRT-compatible method that allows very
493 rapid determining of spatio-temporal parameters of travelling ionospheric
494 disturbances. By using our method, one can obtain instantaneous velocity maps for
495 ionospheric perturbations, and to estimate the position of the source. In addition, also
496 for the first time, we present real-time travel-time diagrams. We demonstrate the
497 performance of our methods on CTID generated by the Tohoku-oki Earthquake of 11
498 March 2011 and the Sanriku-oki Earthquake of 9 March 2011. We use high-rate 1Hz

499 GPS data from the Japan network GEONET for these two earthquakes, and we
500 observe the evolution of the CTID over the source area as it could have been seen in
501 real-time. We show that there is a significant difference between CTID generated by
502 M9 and M7.3 earthquakes in terms of CTID velocities and evolution: the giant
503 Tohoku earthquake generated a massive TEC response in both amplitude and
504 spatial extent, and such a difference can be clearly seen in our results.

505 It is important to emphasize that, besides CTID, our method can detect and
506 analyze other TID that often occur and propagate in the ionosphere. Therefore, the
507 D1-GNSS-RT method can be used for near-real-time Space Weather applications.

508

509

510 **References:**

- 511 1. Astafyeva, E. Ionospheric detection of natural hazards. *Reviews of Geophysics*
512 **57(4)**, 1265-1288 (2019). <https://doi.org/10.1029/2019RG000668>
- 513 2. Meng, X., Vergados, P., Komjathy, A., & Verkhoglyadova, O. Upper
514 atmospheric responses to surface disturbances: An observational perspective.
515 *Radio Science* **54**, 1076– 1098 (2019). <https://doi.org/10.1029/2019RS006858>
- 516 3. Lognonné, P *et al.* Ground-based GPS imaging of ionospheric post-seismic
517 signal. *Planetary and Space Science* **54**, 528–540 (2006)
- 518 4. Astafyeva, E., Heki, K., Afraimovich, E., Kiryushkin, V. & Shalimov, S. Two-
519 mode long-distance propagation of coseismic ionosphere disturbances. *J. Geophys.*
520 *Research - Space Physics.* **114**, A10307 (2009).
521 <https://doi.org/10.1029/2008JA013853>
- 522 5. Rolland, L. *et al.* The resonant response of the ionosphere imaged after the
523 2011 Tohoku-oki earthquake. *Earth Planets Space*, **63(7)**, 62 (2011).
524 <https://doi.org/10.5047/eps.2011.06.020>
- 525 6. Liu, J.-Y *et al.* Ionospheric disturbances triggered by the 11 March 2011 M9.0
526 Tohoku earthquake. *J. Geophys. Res.* **116**, A06319 (2011).
527 <https://doi.org/10.1029/2011JA016761>
- 528 7. Occhipinti, G. The seismology of the planet Mongo: The 2015 ionospheric
529 seismology review. *Subduction Dynamics: From Mantle Flow to Mega Disasters*,
530 169-182 (2015).

- 531 8. Calais, E., & Minster, J.B. GPS detection of ionospheric perturbations following
532 the January 17, 1994, Northridge earthquake. *Geophys. Res. Lett.* **22**, 1045-1048
533 (1995). <https://doi.org/10.1029/95GL00168>
- 534 9. Heki, K. Explosion energy of the 2004 eruption of the Asama Volcano, central
535 Japan, inferred from ionospheric disturbances. *Geophys. Res. Lett.* **33**, L14303
536 (2006). <https://doi.org/10.1029/2006GL026249>
- 537 10. Afraimovich, E., Feng, D., Kiryushkin, V. & Astafyeva, E. Near-field TEC
538 response to the main shock of the 2008 Wenchuan earthquake. *Earth, Planets,*
539 *Space.* **62(11)**, 899-904 (2010). <https://doi.org/10.5047/eps.2009.07.002>
- 540 11. Kiryushkin, V.V., Afraimovich, E.L. & Astafyeva, E.I. The evolution of seismo-
541 ionospheric disturbances according to the data of dense GPS network. *Cosmic*
542 *Research* **49(3)**, 227-239 (2011). <https://doi.org/10.1134/S0010952511020043>
- 543 12. Bagiya, M.S., Sunil, P.S., Sunil, A.S., & Ramesh, D. S. Coseismic contortion
544 and coupled nocturnal ionospheric perturbations during 2016 Kaikoura, Mw7.8 New
545 Zealand earthquake. *J. Geophys. Res. Space Physics* **123**, 1477–1487 (2018).
546 <https://doi.org/10.1002/2017JA024584>
- 547 13. Afraimovich, E. L., Astafyeva, E. I. & Kiryushkin, V.V. Localization of the source
548 of ionospheric disturbance generated during an earthquake. *International Journal of*
549 *Geomagnetism and Aeronomy* **6(2)**, 2002 (2006).
550 <https://doi.org/10.1029/2004GI000092>
- 551 14. Astafyeva, E., Lognonné, P. & Rolland, L. First ionosphere images for the
552 seismic slip on the example of the Tohoku-oki earthquake. *Geophys. Res. Lett.* **38**,
553 L22104 (2011). <https://doi.org/10.1029/2011GL049623>
- 554 15. Astafyeva, E., Rolland, L., Lognonné, P., Khelifi, K. & Yahagi, T. Parameters of
555 seismic source as deduced from 1Hz ionospheric GPS data: case-study of the 2011
556 Tohoku-oki event. *J. Geophys. Res.* **118(9)**, 5942-5950 (2013).
557 <https://doi.org/10.1002/jgra50556>
- 558 16. Tsai, HF., Liu, JY., Lin, CH. & Chen, CH. Tracking the epicenter and the
559 tsunami origin with GPS ionosphere observation. *Earth, Planets and Space* **63(7)**,
560 859–862 (2011). <https://doi.org/10.5047/eps.2011.06.024>
- 561 17. Shults, K., Astafyeva, E. & Adourian, S. Ionospheric detection and localization
562 of volcano eruptions on the example of the April 2015 Calbuco events. *J. Geophys.*
563 *Res.-Space Physics* **121(10)**, 10303-10315 (2016).
564 <https://doi.org/10.1002/2016JA023382>

- 565 18. Lee, R.F., Rolland, L.M. & Mykesell, T.D. Seismo-ionospheric observations,
566 modeling and backprojection of the 2016 Kaikoura earthquake. *Bulletin of the*
567 *Seismological Society of America*. **108(3B)**, 1794–1806 (2018).
568 <https://doi.org/10.1785/0120170299>
- 569 19. Bagiya, M.S. *et al.* The Ionospheric view of the 2011 Tohoku-Oki earthquake
570 seismic source: the first 60 seconds of the rupture. *Scientific Reports*. **10**, 5232
571 (2020). <https://doi.org/10.1038/s41598-020-61749-x>
- 572 20. Kamogawa, M. *et al.* A possible space-based tsunami early warning system
573 using observations of the tsunami ionospheric hole. *Scientific Reports*, **6(1)**, 37989,
574 (2016). <https://doi.org/10.1038/srep37989>
- 575 21. Manta, F., Occhipinti, G., Feng, L. & Hill, E.M. Rapid identification of
576 tsunamigenic earthquakes using GNSS ionospheric sounding. *Sci Rep* **10**, 11054
577 (2020). <https://doi.org/10.1038/s41598-020-68097-w>
- 578 22. Savastano, G. *et al.* Real-time detection of tsunami ionospheric disturbances
579 with a stand-alone GNSS-receiver: a preliminary feasibility demonstration. *Sci.*
580 *Reports*, **7**, 46607 (2017). <https://doi.org/10.1038/srep46607>
- 581 23. Shrivastava, M.N. *et al.* Tsunami detection by GPS-derived ionospheric total
582 electron content. *Sci. Rep.* **11**, 12978 (2021). [https://doi.org/10.1038/s41598-021-](https://doi.org/10.1038/s41598-021-92479-3)
583 [92479-3](https://doi.org/10.1038/s41598-021-92479-3)
- 584 24. Ravanelli, M. *et al.* GNSS total variometric approach: first demonstration of a
585 tool for real-time tsunami genesis estimation. *Sci Rep* **11**, 3114 (2021).
586 <https://doi.org/10.1038/s41598-021-82532-6>
- 587 25. Hofmann-Wellenhof, B., Lichtenegger, H. & Wasle, E. *GNSS-Global Navigation*
588 *Satellite Systems*. (Springer, Vienna, 2008) [https://doi.org/10.1007/978-3-211-](https://doi.org/10.1007/978-3-211-73017-1)
589 [73017-1](https://doi.org/10.1007/978-3-211-73017-1)
- 590 26. Nava, B., Radicella, S., Leitinger, R. & Coïsson, P. A near-real-time model-
591 assisted ionosphere electron density retrieval method. *Radio Sci.* **41**, RS6S16.
592 (2006).
- 593 27. Bilitza, D. *et al.* International Reference Ionosphere 2016: From ionospheric
594 climate to real-time weather predictions. *Space Weather*, **15**, 418–429. (2017)
595 <https://doi.org/10.1002/2016SW001593>
- 596 28. Astafyeva, E. & Shults, K. Ionospheric GNSS imagery of seismic source:
597 possibilities, difficulties, challenges. *J. Geophys. Res.* **124(1)**, 534-543 (2019).
598 <https://doi.org/10.1029/2018JA026107>

- 599 29. Heki, K., & Ping, J. Directivity and apparent velocity of the coseismic
600 ionospheric disturbances observed with a dense GPS array. *Earth and Planetary*
601 *Science Letters*, **236**, 845–855. (2005)
- 602 30. Komjathy, A. *et al.* Detecting ionospheric TEC perturbations caused by natural
603 hazards using a global network of GPS receivers: The Tohoku case study. *Earth*
604 *Planets Space* **64**, 1287–1294. (2012). <https://doi.org/10.5047/eps.2012.08.003>
- 605 31. Galvan, D. A. *et al.* Ionospheric signatures of Tohoku-Oki tsunami of March 11,
606 2011: Model comparisons near the epicenter. *Radio Sci.* **47**, RS4003 (2012).
607 <https://doi.org/10.1029/2012RS005023>
- 608 32. Melgar, D. *et al.* Earthquake magnitude calculation without saturation from the
609 scaling of peak ground displacement. *Geophys. Res. Lett.* **42**, 5197–5205. (2015)
610 <https://doi.org/10.1002/2015GL064278>
- 611 33. Afraimovich, E.L., Palamartchouk, K.S. & Perevalova, N.P. GPS radio
612 interferometry of travelling ionospheric disturbances. *Journal of Atmospheric and*
613 *Solar-Terrestrial Physics*. **60(12)**, 1205-1223 (1998). [https://doi.org/10.1016/S1364-](https://doi.org/10.1016/S1364-6826(98)00074-1)
614 [6826\(98\)00074-1](https://doi.org/10.1016/S1364-6826(98)00074-1)
- 615 34. Afraimovich, E.L., Perevalova, N.P., Plotnikov, A.V. & Uralov, A.M. The shock-
616 acoustic waves generated by earthquakes. *Ann. Geophys.* **19**, 395–409 (2001).
617 <https://doi.org/10.5194/angeo-19-395-2001>
- 618 35. Garrison, J. L., Lee, S.-C. G., Haase, J. S., & Calais, E. A method for detecting
619 ionospheric disturbances and estimating their propagation speed and direction
620 using a large GPS network. *Radio Sci.* **42**, RS6011 (2007).
621 <https://doi.org/10.1029/2007RS003657>
- 622 36. Afraimovich, E.L., & Perevalova, N.P. *GPS monitoring of the Earth's upper*
623 *atmosphere*. (SC RRS SB RAMS, Irkutsk, Russia, in Russian, 2006)
- 624 37. Rolland, L. M. *et al.* Discriminating the tectonic and non-tectonic contributions in
625 the ionospheric signature of the 2011, M_w 7.1, dip-slip Van earthquake, Eastern
626 Turkey. *Geophys. Res. Lett.* **40**, 2518–2522 (2013).
627 <https://doi.org/10.1002/grl.50544>
- 628 38. Astafyeva, E., Rolland, L.M. & Sladen, A. Strike-slip earthquakes can also be
629 detected in the ionosphere. *Earth and Planetary Science Letters* **V.405**, 180-193.
630 (2014). <https://doi.org/10.1016/j.epsl.2014.08.024>
- 631 39. Bagiya, M. S. *et al.* Efficiency of coseismic ionospheric perturbations in
632 identifying crustal deformation pattern: Case study based on M_w 7.3 May Nepal

633 2015 earthquake. *J. Geophys. Res. Space Physics* **122**, 6849-6857 (2017)
634 <https://doi.org/10.1002/2017JA024050>

635 40. Bagiya, M.S. *et al.* Mapping the Impact of Non-Tectonic Forcing mechanisms
636 on GNSS measured Coseismic Ionospheric Perturbations. *Sci. Rep.* **9**, 18640
637 (2019). <https://doi.org/10.1038/s41598-019-54354-0>

638 41. Hayes, G.P. The finite, kinematic rupture properties of great-sized earthquakes
639 since 1990. *Earth Planet. Sci. Lett.* **468**, 94-100 (2017).
640 <https://doi.org/10.1016/j.epsl.2017.04.003>

641 42. Simons, M. *et al.* The 2011 magnitude 9.0 Tohoku-oki earthquake: Mosaicking
642 the megathrust from seconds to centuries. *Science* **332(6036)**, 1421–1425. (2011).
643 <https://doi.org/10.1126/science.1206731>

644 43. Bletery, Q., Sladen, A., Delouis, B., Vallée, M., Nocquet, J.-M., Rolland, L., &
645 Jiang, J. A detailed source model for the Mw9.0 Tohoku-Oki earthquake reconciling
646 geodesy, seismology and tsunami records. *Journal of Geophysical Research: Solid*
647 *Earth* **119**, 7636–7653. (2014). <https://doi.org/10.1002/2014JB011261>

648 44. Shao, G., Ji, C., & Zhao, D. Rupture process of the 9 March, 2011 Mw 7.4
649 Sanriku-Oki, Japan earthquake constrained by jointly inverting teleseismic
650 waveforms, strong motion data and GPS observations. *Geophysical Research*
651 *Letters* **38**, L00G20. (2011) <https://doi.org/10.1029/2011GL049164>

652 45. Kakinami, Y. *et al.* Tsunamigenic ionospheric hole. *Geophys. Res. Lett.* **39**,
653 L00G27 (2012). <https://doi.org/10.1029/2011GL050159>

654 46. Astafyeva, E., Shalimov, S., Olshanskaya, E. & Lognonné, P. Ionospheric
655 response to earthquakes of different magnitudes: larger quakes perturb the
656 ionosphere stronger and longer. *Geophys. Res. Lett.* **40(9)**, 1675-1681 (2013).
657 <https://doi.org/10.1002/grl.50398>

658 47. Cahyadi, M.N. & Heki, K. Coseismic ionospheric disturbance of the large strike-
659 slip earthquakes in North Sumatra in 2012: M_w dependence of the disturbance
660 amplitudes. *Geophysical Journal International* **200(1)**, 116–129 (2015).
661 <https://doi.org/10.1093/gji/ggu343>

662 48. Thomas, D. *et al.* Revelation of early detection of co-seismic ionospheric
663 perturbations in GPS-TEC from realistic modelling approach: Case study. *Sci Rep*
664 **8**, 12105 (2018). <https://doi.org/10.1038/s41598-018-30476-9>

- 665 49. Krishnamoorthy S. *et al.* Aerial Seismology Using Balloon-Based Barometers.
666 *IEEE Transactions on Geoscience and Remote Sensing* **57(12)**, 10191-10201
667 (2019) <https://doi.org/10.1109/TGRS.2019.2931831>
- 668 50. Hadas, T. & Bosy, J. IGS RTS precise orbits and clocks verification and quality
669 degradation over time. *GPS Solut* **19**, 93–105 (2015).
670 <https://doi.org/10.1007/s10291-014-0369-5>
- 671 51. RTCM. *Radio Technical Commission for Maritime Services*.
672 <https://www.rtcn.org/> (2020).
- 673 52. GNSS Science Support Centre, ESA. *Networked Transport of RTCM via*
674 *Internet Protocol*. [https://gssc.esa.int/wp-](https://gssc.esa.int/wp-content/uploads/2018/07/NtripDocumentation.pdf)
675 [content/uploads/2018/07/NtripDocumentation.pdf](https://gssc.esa.int/wp-content/uploads/2018/07/NtripDocumentation.pdf) (2020).
- 676 53. Takasu, T. RTKLIB: an open source program package for GNSS positioning.
677 <http://www.rtklib.com> (2013)
- 678 54. Noll, Carey E. The Crustal Dynamics Data Information System: A resource to
679 support scientific analysis using space geodesy. *Advances in Space Research*.
680 **45(12)**, 1421-1440, (2010). <http://dx.doi.org/10.1016/j.asr.2010.01.018>
- 681 55. Wessel, P. *et al.* The Generic Mapping Tools version 6. *Geochemistry,*
682 *Geophysics, Geosystems* **20**, 5556–5564, (2019).
683 <https://doi.org/10.1029/2019GC008515>

684

685 **Acknowledgements**

686 We thank the French Space Agency (CNES, Project “IMAGION”) for the support. BM
687 additionally thanks the CNES and the IPGP for the PhD fellowship and the support of
688 the RFBR, grant No. 19-05-00889, and partly by budgetary funding of Basic
689 Research Program II.16.

690

691 **Author contributions statement**

692 B.M. developed the codes, made the figures and wrote the first draft of the
693 Manuscript. E.A. conceived the idea of the study, participated in developing of the
694 methods and in the writing of the Manuscript. All authors discussed the results and
695 reviewed the final version of the Manuscript.

696

697 **Competing interests**

698 The authors declare no competing interests.

699

700 **Competing financial interests:** The authors declare no competing financial
701 interests.

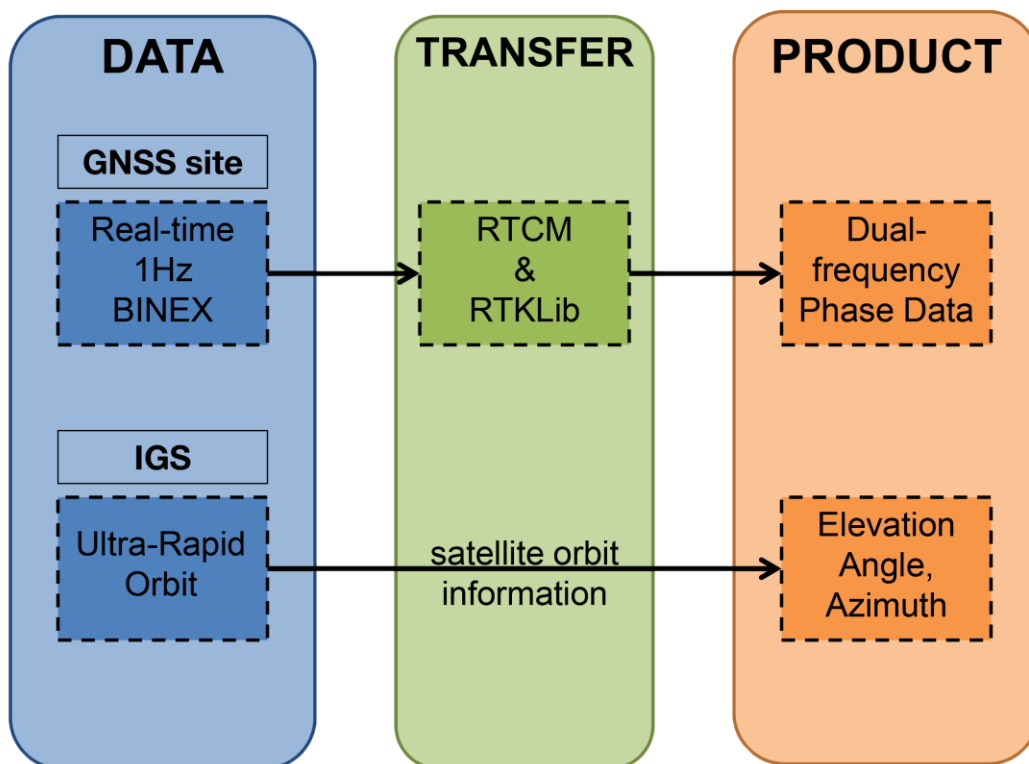
702

703 **Data availability**

704 The data are available from the GeoSpatial Authority of Japan (GSI, terras.go.jp).
705 http://datahouse1.gsi.go.jp/terras/terras_english.html

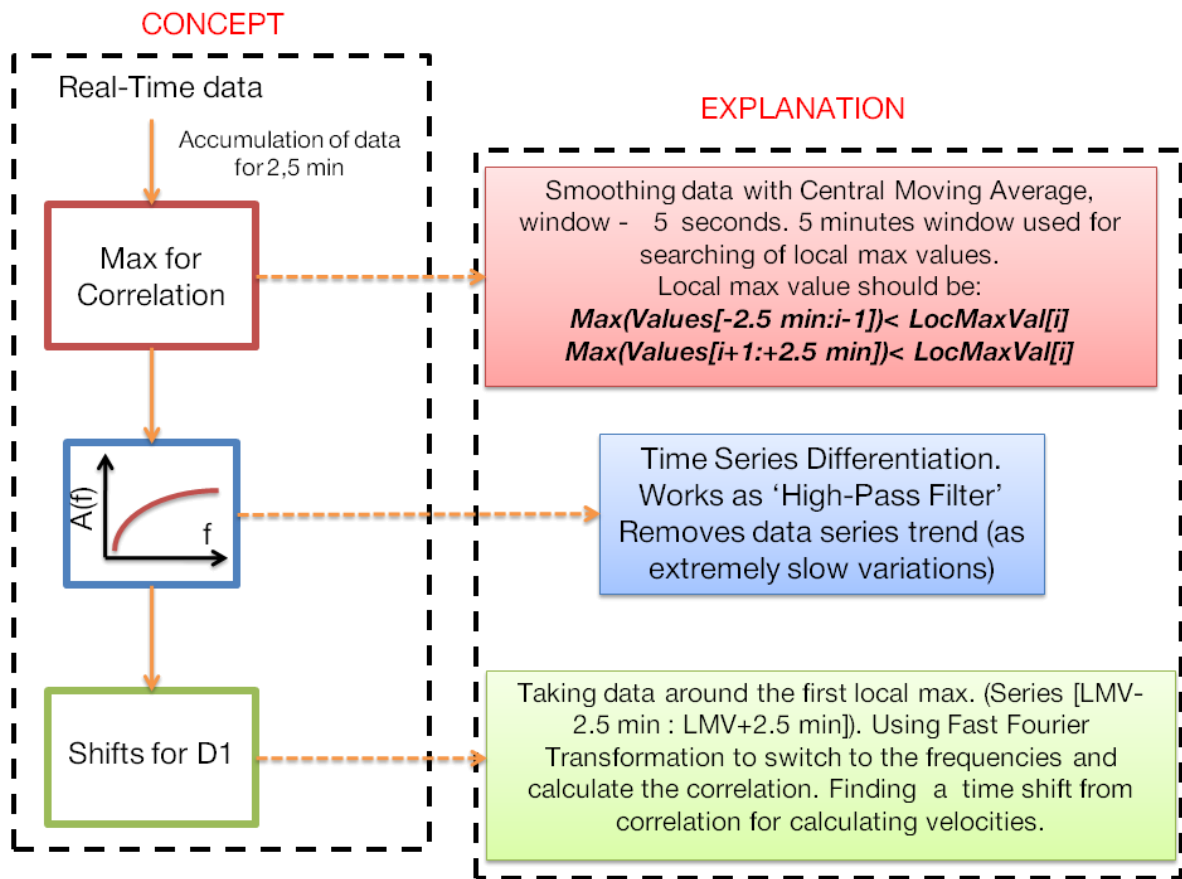
706

707 **Figures**



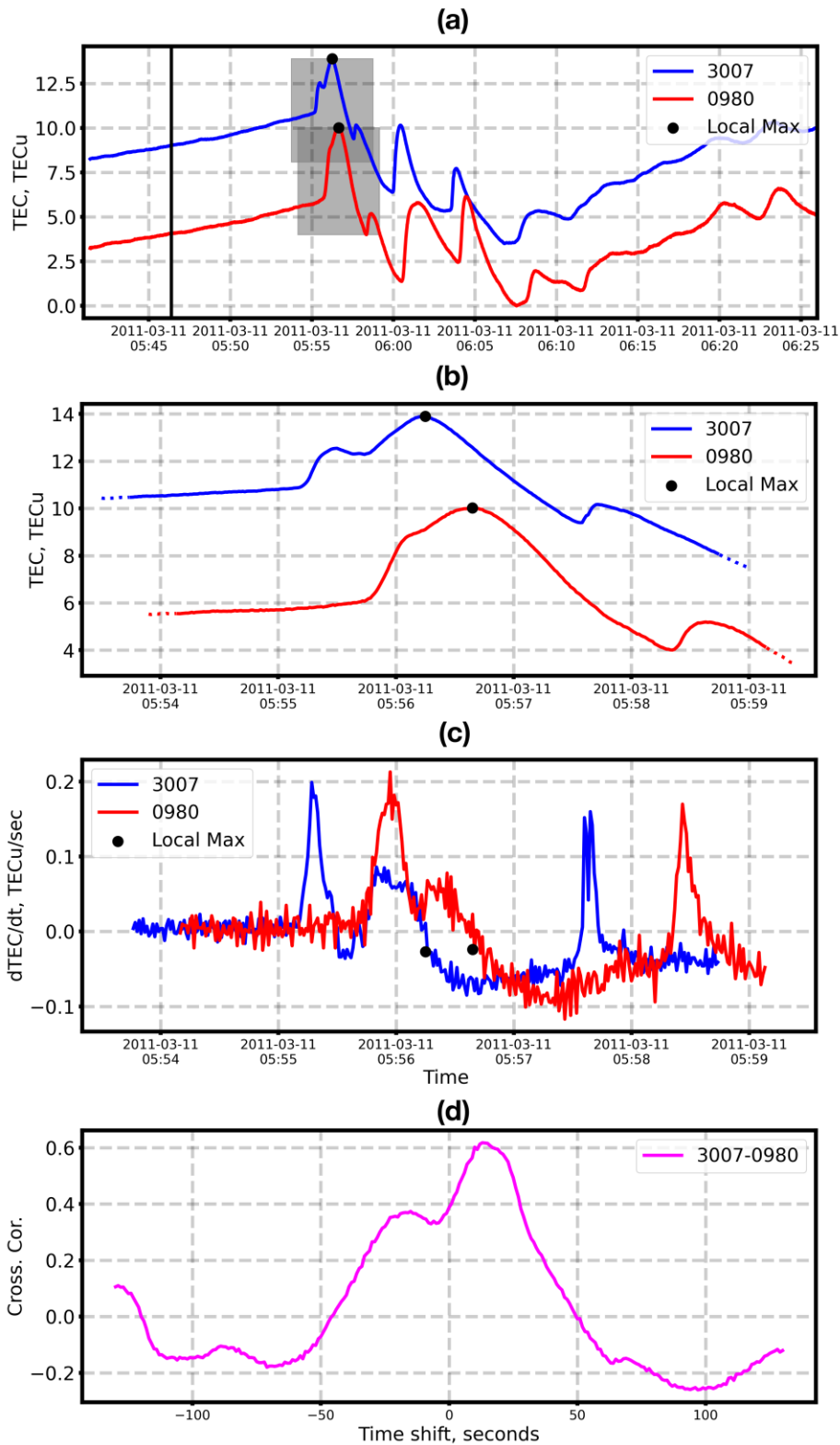
708

709 **Figure 1.** Real-time collection of GNSS phase data and orbit parameters. Networked
710 Transport of RTCM [51] via Internet Protocol (NTRIP) [52] could be used to provide
711 the real-time data stream from the given stations. The main goal of the protocol is
712 Real Time Kinematics (RTK), but it is also suitable for our purposes since it transfers
713 dual-frequency phase and pseudo-range data in real time. RTKLib [53] software
714 could be used to convert binary information from NTRIP data stream. The
715 International GNSS Service (IGS) ultra-rapid orbit [54] is used to obtain the
716 information about the elevation angle and the azimuth. BINEX – Binary INdependent
717 EXchange format for files that is used in real-time.



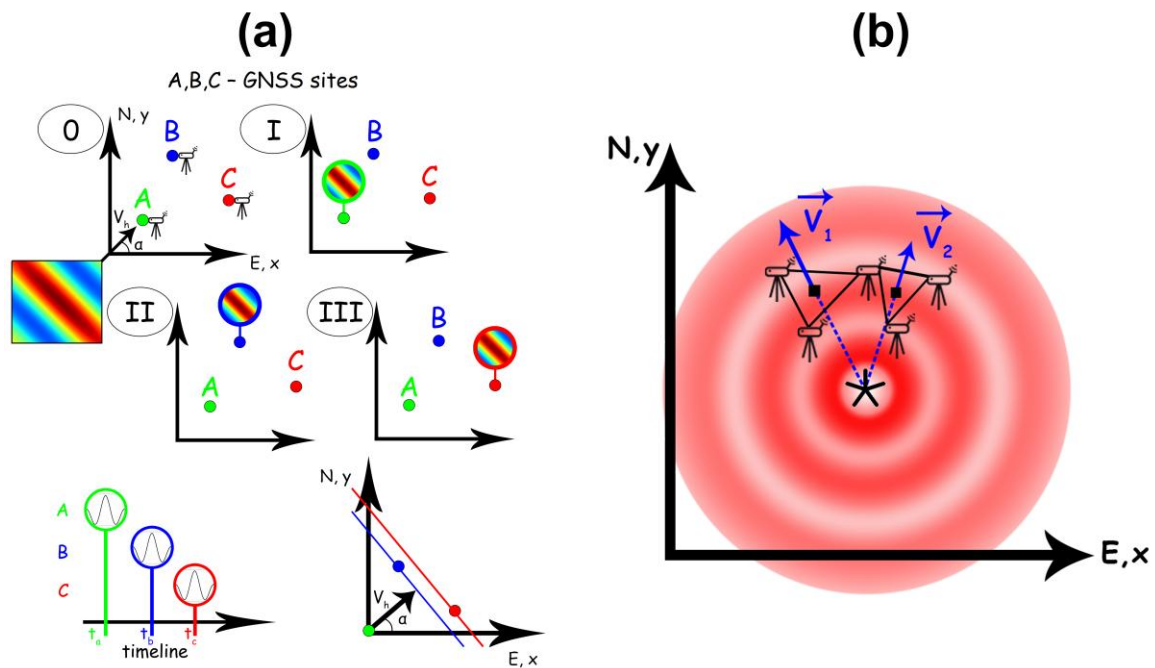
718
719
720
721

Figure 2. The concept of the near-real-time detection of CTID and TID, and explanation of the main steps of the procedure.



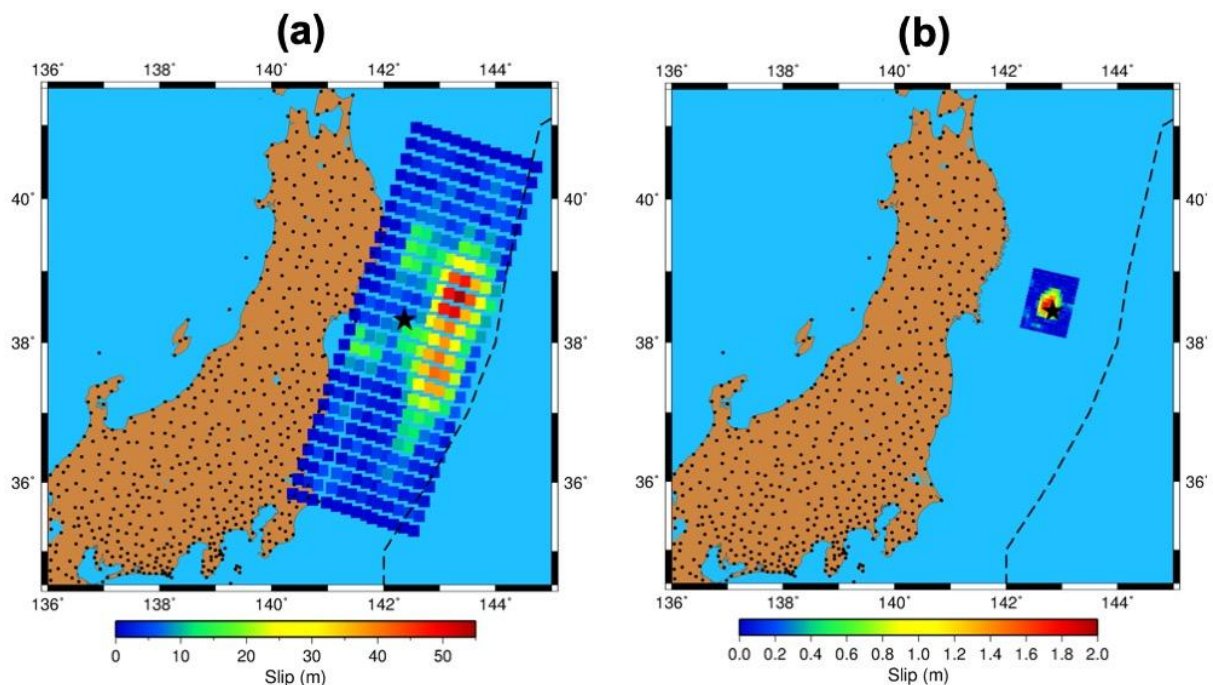
722
723
724
725
726
727
728
729

Figure 3. (a) Variations of slant TEC registered by GPS satellite 26 at stations 0980 and 3007 following the Tohoku earthquake of 11 March 2011. The earthquake time is indicated by vertical black line. Gray shaded rectangles denote 5-min time window, which is used for further cross-correlation analysis; (b) sTEC variations within 5-min time window; (c) dTEC/dt within 5-min time window. Black point shows the LMV determined from the sTEC data. The data are 1Hz; (d) Cross-correlation function for the two dTEC/dt time series



730

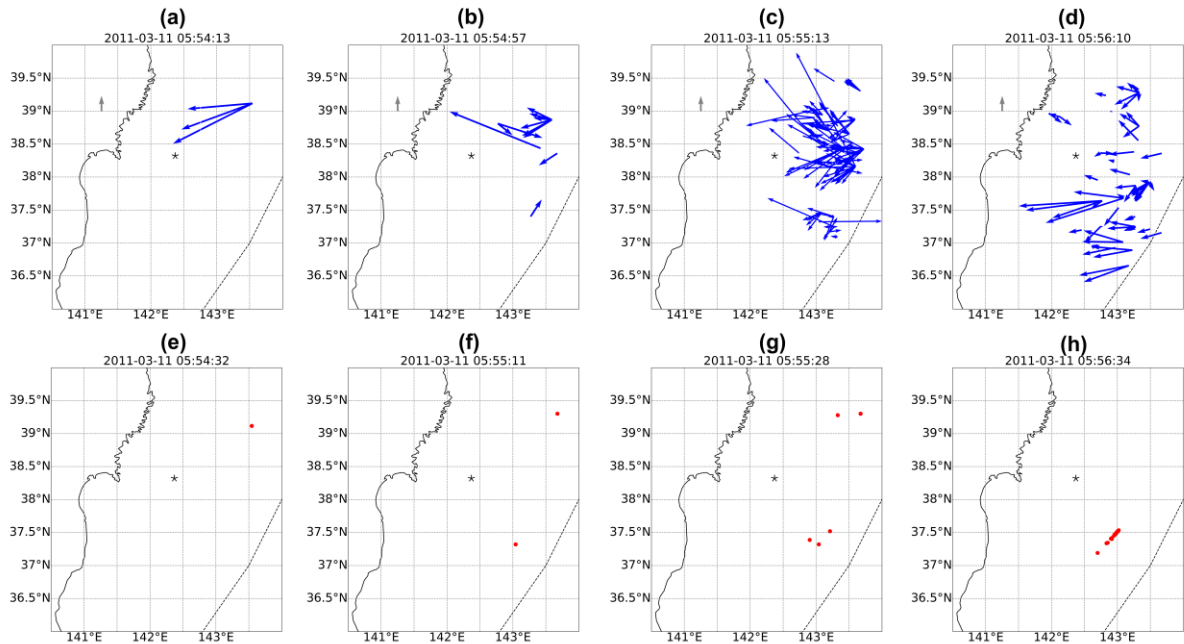
731 **Figure 4. (a)** Explanation of D1 technique. A, B, C – GNSS stations that are used to
 732 determine the CSID parameters: horizontal velocity (v_h) and azimuth (α). 0, I, II, III
 733 mark the moments of time when the perturbation approaches the detection triangle
 734 (0) and when the perturbation is detected at points A, B, and C, respectively. The
 735 wavefront is considered to be plain; **(b)** Ionospheric localization of CTIDs based on
 736 the known location and values of two velocity vectors V_1 and V_2 .
 737



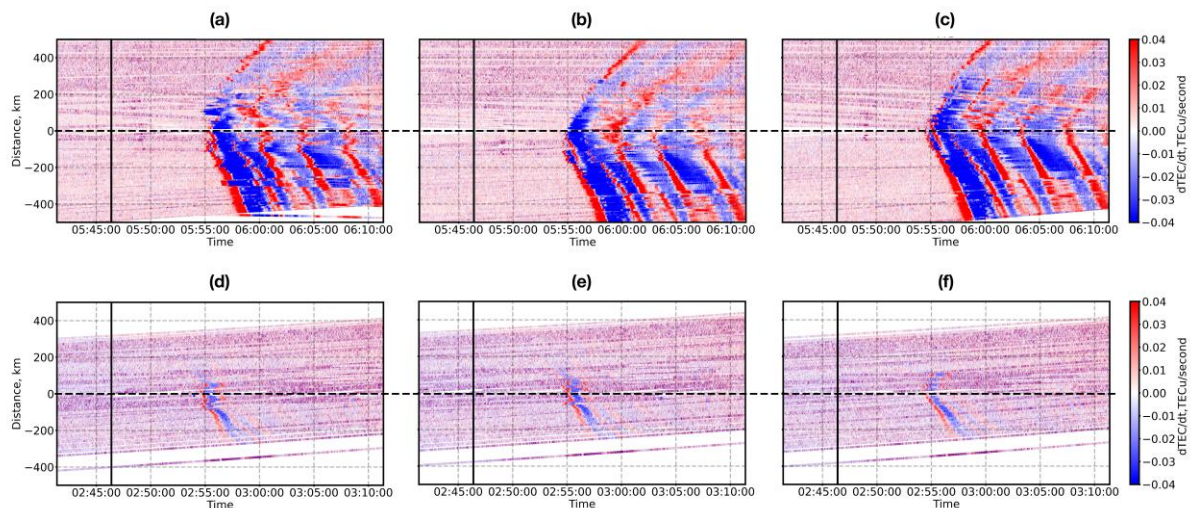
738

739 **Figure 5.** Maps for the Mw9.0 Tohoku earthquake of 11 March 2011 **(a)** and the
 740 M7.3 Sanriku earthquake of 9 March 2011 **(b)**. Black star shows the epicenter, black
 741 dots show GPS receivers, and the colored squares depict the amplitude of the co-
 742 seismic slip that occurred due to the earthquakes as calculated by the NEIC USGS
 743 [37]. The corresponding color scale is shown on the bottom. The dotted curve shows

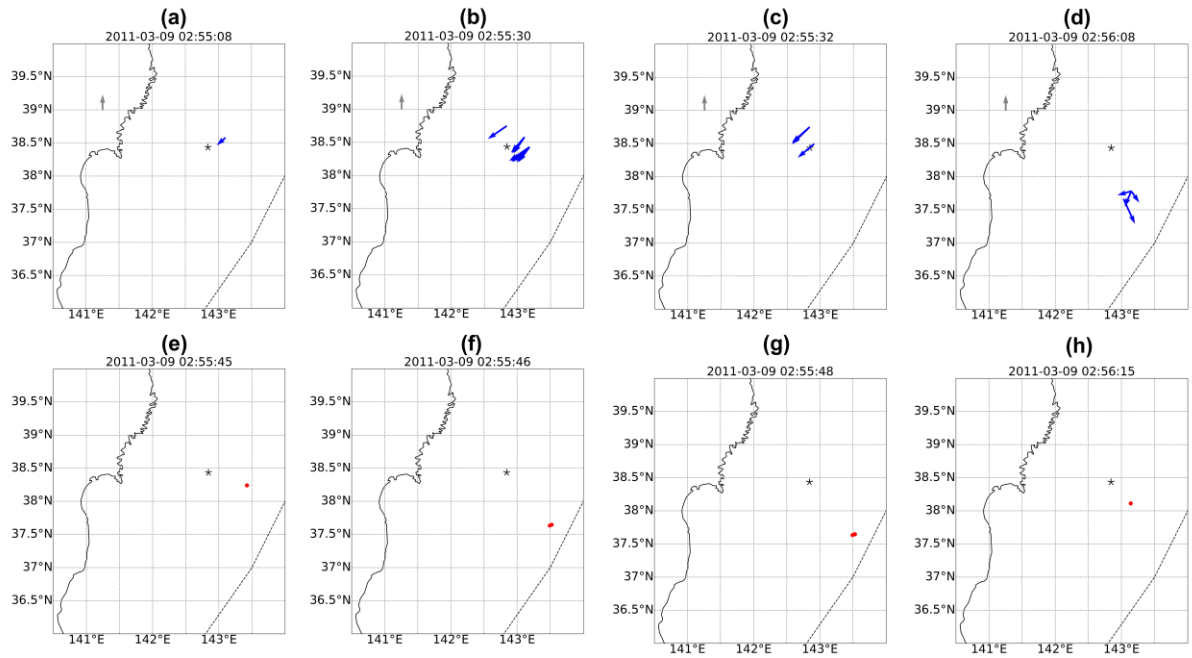
744 the position of the Japan Trench. The maps were plotted by using GMT6 software
 745 [55]
 746



747
 748 **Figure 6.** (a-d) CTID velocity field calculated from the first CTID detected by GPS
 749 satellite PRN 26 after the Tohoku earthquake. The dotted curve shows the position of
 750 the Japan Trench, black star depicts the epicenter. The gray arrow corresponds to
 751 1,1 km/s; (e-h) localization of the seismic source as estimated from the first velocity
 752 vectors shown on panels (a-d).
 753

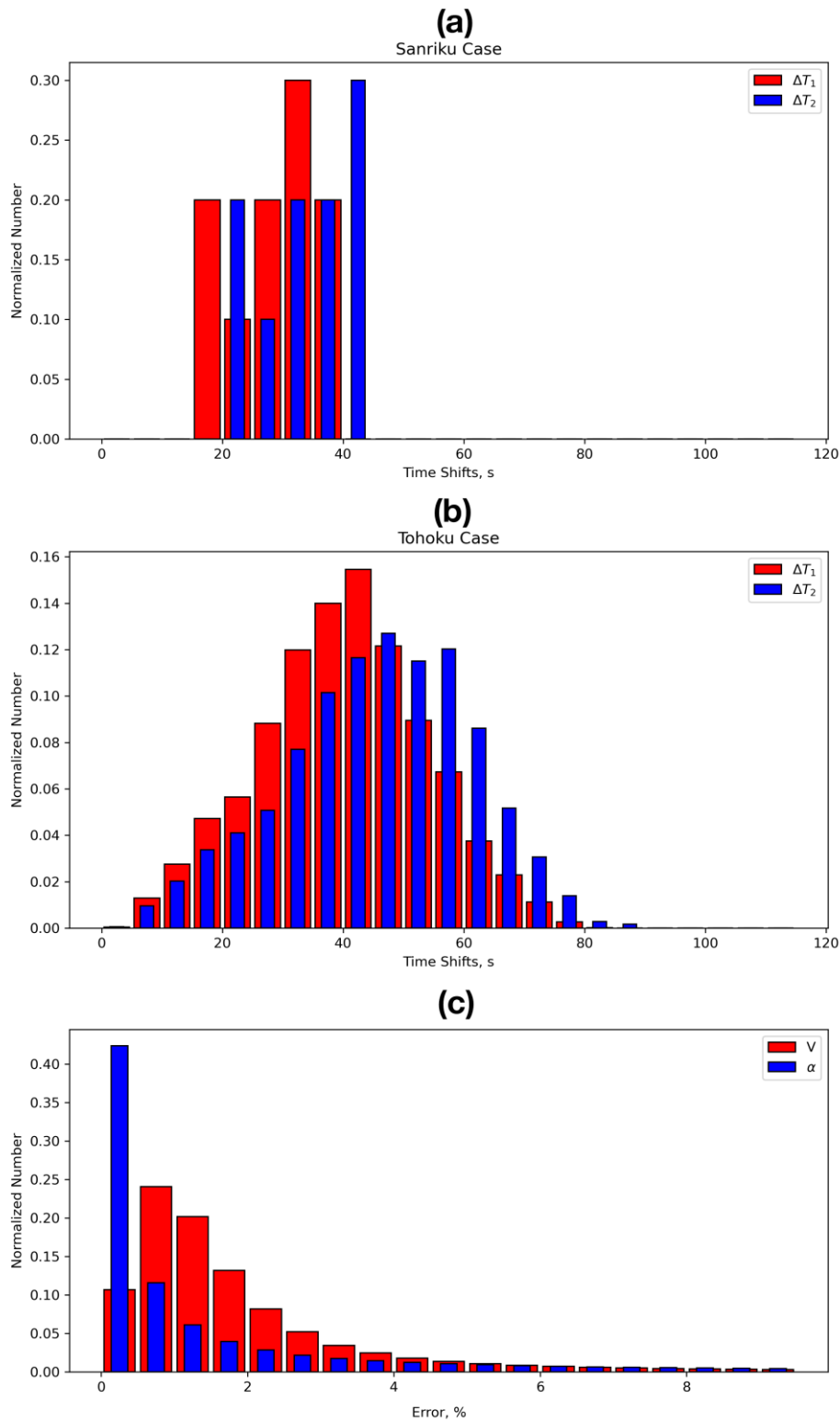


754
 755 **Figure 7.** Near-real-time travel time diagram (NRT-TTD) plotted by using $dTEC/dt$
 756 data for the Tohoku (a, b, c) earthquake (satellite G26) and Sanriku (d, e, f)
 757 earthquake (satellite G07). In panels (a, d) the distance is calculated with respect to
 758 the earthquakes' epicenters as estimated by the USGS, in panels (b, e) – with
 759 respect to the maximum co-seismic uplifts; (c, f) - with respect to the ionospheric
 760 localization as shown in Figures 5(d-e) and 6(d-e). The color scale is shown on the
 761 right.
 762



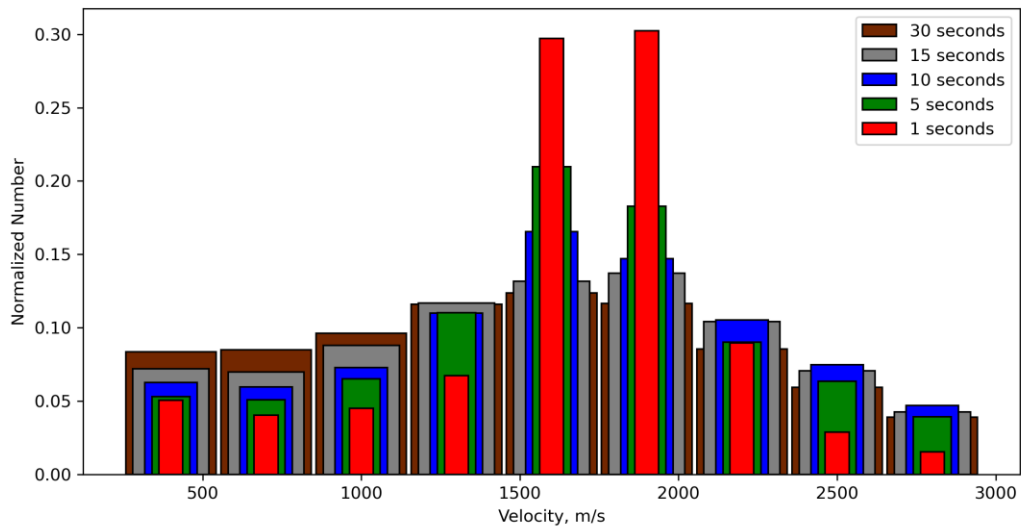
763
 764
 765
 766
 767
 768
 769

Figure 8. (a-d) CTID velocity field calculated from the first CTID detected by GPS satellite PRN 07 following the Sanriku earthquake. The dotted curve shows the position of the Japan Trench, black star depicts the epicenter. The gray arrow corresponds to 1,1 km/s; (e-h) localization of the seismic source as estimated from the first velocity vectors shown on panels (a-d).



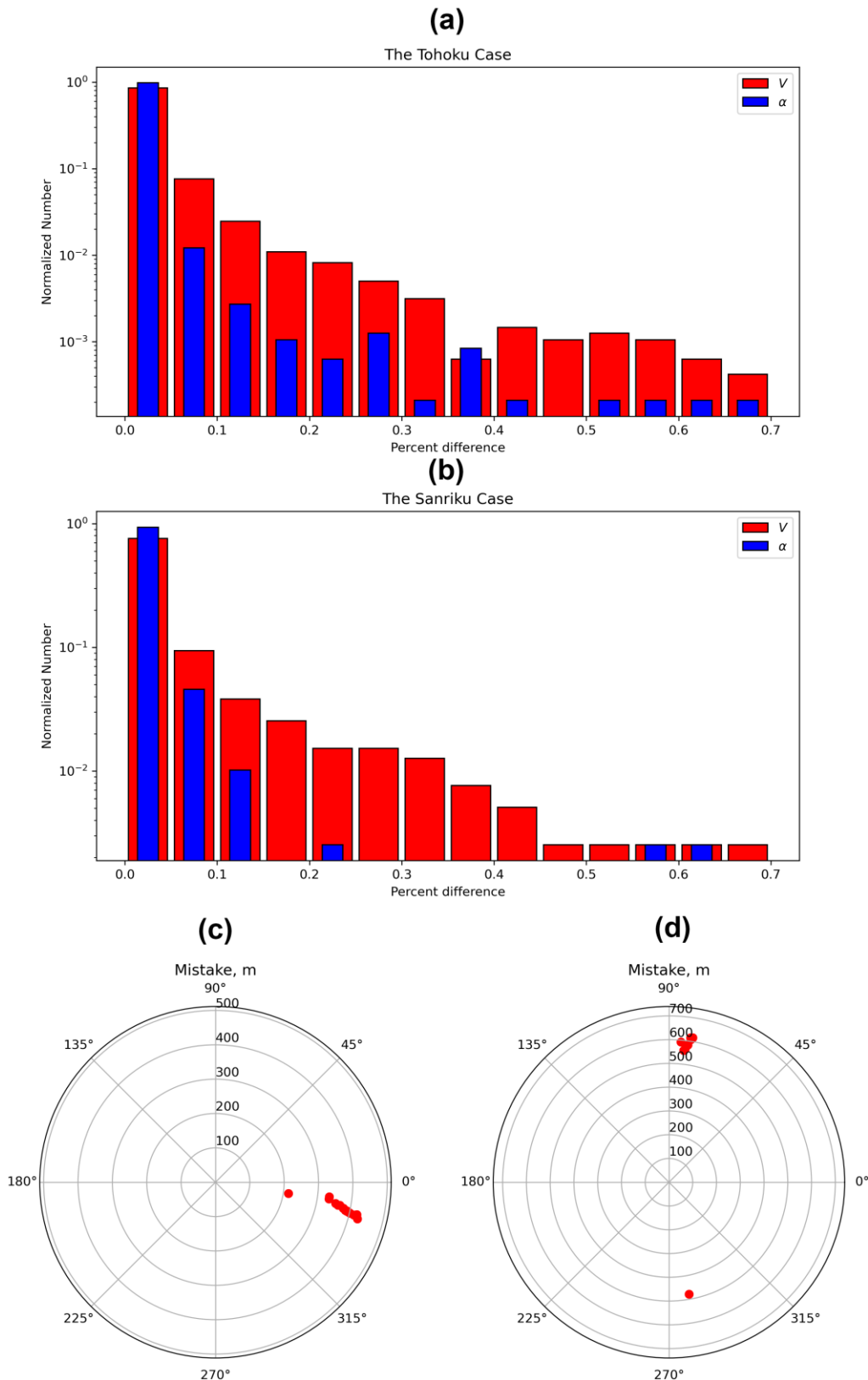
770
771
772
773
774
775

Figure 9. (a-b) Distribution of normalized number of the time shifts between points A-B (red, ΔT_1) and A-C (blue, ΔT_2) of a triangle for the Tohoku (a) and Sanriku (b) earthquakes; **(c)** impact of an error of ± 0.5 seconds on arrival times affects the computation of the velocities values and azimuths.



776
777
778
779

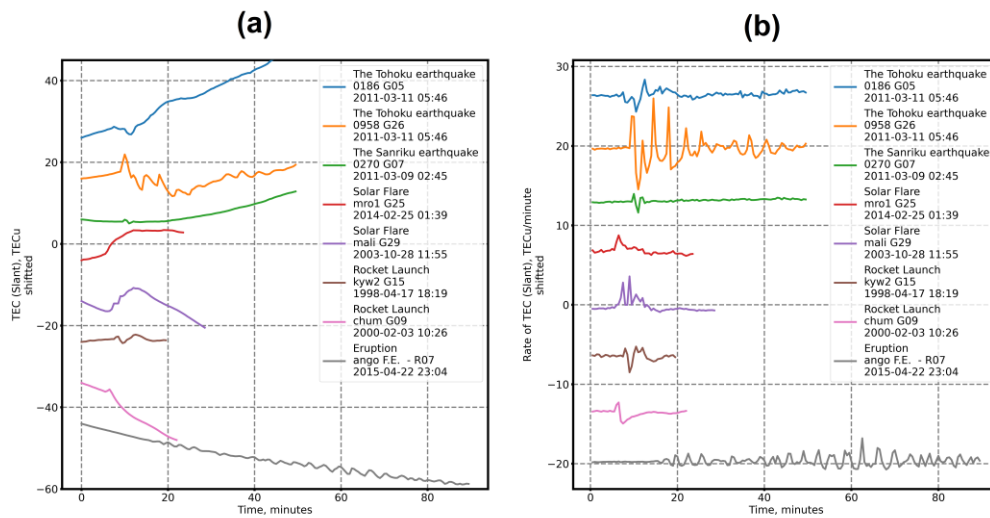
Figure 10. Distribution of velocity values calculated from data of different temporal cadences: 1- (red), 5- (green), 10- (blue), 15- (gray), 30- (brown) seconds.



780
781
782
783
784
785

Figure 11. Accuracy comparison based on different sources of the orbits: navigational RINEX file and ultra-rapid orbits. Panel **(a)** - distribution of percentage difference of amplitude and azimuth of propagation for the Tohoku case (y-axis logarithmic scale); panel **(b)** - distribution of percentage difference of amplitude and azimuth of propagation for the Sanriku case (y-axis logarithmic scale); panel **(c)** -

786 radar diagram of source location difference for the Tohoku case; panel (d) - radar
 787 diagram of source location difference for the Sanriku case.
 788



789 **Figure 12.** Examples of TEC disturbances of different origin that are detectable by
 790 our approach. Panel (a) – slant TEC values characterized by high changes, panel (b)
 791 – Rate of TEC of the exact data series.
 792
 793